Flow Turbulence Combust
DOI 10.1007/s10494-015-9638-9

Particle Velocity and Acceleration in Turbulent Bent Pipe Flows

Azad Noorani[1] · Gaetano Sardina[2] · Luca Brandt[1] · Philipp Schlatter[1]

Received: 29 January 2015 / Accepted: 4 August 2015

Abstract We study the dynamics of dilute micro-size inertial particles in turbulent curved pipe flows of different curvature by means of direct numerical simulations with one-way coupled Lagrangian particle tracking. The focus of this work is on the first and second order moments of the velocity and acceleration of the particulate phase, relevant statistics for any modelling effort, whereas the particle distribution is analysed in a previous companion paper. The aim is to understand the role of the cross-stream secondary motions (Dean vortices) on the particle dynamics. We identify the mean Dean vortices associated to the motion of the particles and show that these are moved towards the side-walls and, interestingly, more intense than those of the mean flow. Analysis of the streamwise particle flux reveals a substantial increase due to the secondary motions that brings particles towards the pipe core while moving them towards the outer bend. The in-plane particle flux, most intense in the flow viscous sub-layer along the side walls, increases with particle inertia and pipe curvature. The particle reflections at the outer bend, previously observed also in other strongly curved configurations, locally alter the particle axial and wall-normal velocity and increase turbulent kinetic energy.

Keywords Curvature effect · Particulate dispersion · Secondary motion · Gas-solid flow · Bent pipe · Particle transport

✉ Azad Noorani
azad@mech.kth.se

[1] Linné FLOW Centre and Swedish e-Science Research Centre (SeRC), KTH Mechanics, Royal Institute of Technology, SE-100 44, Stockholm, Sweden

[2] Department of Meteorology, Stockholm University, 10691 Stockholm, Sweden

Published online: 21 August 2015

1 Introduction

Heat and mass transfer systems such as heat exchangers or pipeline systems are common examples of flow in curved conduits. The curvature leads to an imbalance between the cross-stream pressure gradient and the geometry induced centrifugal forces that causes a secondary motion. A pair of counter-rotating Dean vortices appears in these configurations, which generally enhances mixing and increases heat- and mass-transfer indices. Although this skew-induced secondary motion appears both in turbulent and laminar flows, the fluid flow is typically turbulent in mechanical applications. Turbulent flow in curved pipes may be laden with a solid particulate phase in engineering appliances such as membrane filtration systems or mixing devices in pharmaceutical industries. The dispersed solid particles are subject to the wall-turbulence of the carrier phase, geometry-induced centrifugal forces and the ensuing secondary motion. Due to the geometrical complexity, investigations on complex two-phase phenomena in bent pipes are therefore rare [26].

Spatially developing bends such as elbows and helically coiled tubes are two distinct types of curved geometries. In the first case, a fully developed flow from a straight pipe enters the bend, whereas the flow is fully developed inside the curved geometry in the latter one. Additional torsion (resulting from the coil pitch) acts alongside the centrifugal forces in the latter category. For sufficiently small values of the ratio of coil pitch over coil diameter, the influence of the torsion becomes negligible and the geometry reduces to a torus. Such abstraction – a continuously curved pipe configuration – provides a unique opportunity to isolate the effect of the curvature on the turbulent characteristics, but also to study the influence of the centrifugal forces and of the secondary motion on the near-wall dynamics.

Among the few references about turbulent flow in toroidal pipes, we mention the direct numerical simulation (DNS) by Hüttl & Friedrich [11, 12] and the large eddy simulation (LES) by Boersma & Nieuwstadt [5]. In these studies the effect of the curvature on the mean flow and velocity fluctuations is studied for low curvatures. In the recent work by Noorani et al. [16] DNSs are performed in sufficiently long pipes at moderately high Reynolds numbers such that the flow remains turbulent even in strongly curved configurations. The Reynolds stress budgets are computed for various curvatures and it is shown that the turbulent flow is highly damped in the inner side of the strongly curved pipe while it remains fully turbulent in the outer bend.

As now well understood, the transport of micro-sized inertial particles in wall-bounded turbulent flows is characterised by the so-called turbophoresis, i.e. the accumulations of heavy particles at the wall caused by the turbulence inhomogeneity, in particular by the gradients in the turbulent kinetic energy profiles [21, 30]. Another peculiar phenomenon in the dispersion process of heavier-than-fluid particles is the small-scale clustering: The particles aggregate in specific regions characterised by higher values of the turbulent kinetic energy dissipation rate. As opposed to turbophoresis, the latter phenomenon –commonly known as preferential concentration– appears in all sorts of turbulent flows (homogenous or inhomogeneous) laden with heavy particles (see [2, 25] for review).

In more recent studies, Huang & Durbin [9, 10] address the effect of the geometry induced centrifugal forces on particle clustering in the presence of turbophoretic drifts in a simulation of S-shaped turbulent channel flow with strong curvature. These authors observed thick layers of elevated particle concentration forming in the bend, named as *'reflection layers'*. This feature is a direct consequence of the ballistic behaviour of heavy

particles colliding with a wall. Huang & Durbin [10] present a simplified *toy model* to explain the oscillatory behaviour of the particle concentration. These authors also discuss the erosion induced by wall-particle collisions [9].

The experiments by Wu & Young [28] focus on the wall deposition of inertial particles in spatially developing mildly curved ducts (with rectangular cross-section). These authors report a dramatic increase of the particle accumulation rate at the outer bend compared to a straight configuration and show that heavy inertial particles are driven by centrifugal forces rather than turbophoresis even in a mildly curved configuration. These results may not be directly comparable to the data in a serpentine channel by [10] since absorption at the wall is prescribed rather than elastic rebounds. Simulations of artificial swirl in a spatially developing turbulent straight pipe are presented in Zonta et al. [32]. According to these authors, superposition of centrifugal swirling motions does not disrupt the turbophoretic drift of the particles, but actually enhances the near-wall particle accumulation.

Secondary Dean cells and Görtler vortices appearing in pressure-driven turbulent curved channels and boundary layers are not fixed in the spanwise direction. This leads to an instantaneous nonuniform spanwise particle distribution which is difficult to analyse in terms of preferential concentrations. Bent pipes, conversely, display similar centrifugation and secondary motions but the Dean cells are fixed in space. In this case, the particle concentration reaches a statistically stationary state that can be directly and more easily related to the underlying flow structure. This facilitates modelling of particle-laden turbulent flows in wall-bounded complex geometries [28].

The transport of a micro-size particulate phase in turbulent toroidal pipes was investigated in a companion study by Noorani et al. [17]. In this first investigation (referred to as **bpPart15** in the following) the effect of the curvature on the particle transport and accumulation is examined using DNS of the turbulent flow, and Lagrangian tracking of individual particles in the one-way coupling approximation. The study focuses on the particle distribution and near-wall accumulation when varying the curvature. In addition, near-wall 3D helicoidal particle streaks are observed in both mildly and strongly curved configurations with their inclination varying with the strength of the secondary motion of the carrier phase. Enhancing the pipe curvature alters the particles transport at the wall and in the core of the pipe: depending on the curvature, the central regions of the mean Dean vortices may appear to be completely depleted of particles. Reflection layers, similar to those previously observed in S-shaped channels, also appear in the strongly curved pipe.

Despite previous efforts, the dynamics of particulate dispersions in turbulent flows with large vortical structures where secondary motions and centrifugal force co-exist, is still far from understood. The main objective of the present paper, as an extension of **bpPart15**, is to characterise the dependence of the first and the second order statistical moments of velocity and acceleration on the geometrical curvatures for different particle populations (particle inertia).

In the following, we briefly review the governing equations and numerical method employed here. In Section 3.1 we recall the most important features of mean particle concentration in bent pipes from **bpPart15**, necessary for the analysis discussed later. The statistics of the particle velocity and velocity fluctuations are discussed in Sections 3.2 and 3.3. The in-plane and streamwise fluxes of the solid phase are presented in Section 3.4. The particle acceleration and its variance with curvature are shown in Section 3.5. The paper ends with a summary of the main conclusions.

2 Governing Equations and Numerical Method

The numerical setups is presented in detail in **bpPart15**; nevertheless, a brief overview is given here for clarity.

Figure 1a shows a schematic view of a cross-section of a curved pipe. The toroidal coordinates (R, s, ζ) are shown together with the local (in-plane) poloidal coordinates (r, θ). In the following the subscripts r, θ and s denote the vector components in the radial (wall-normal), azimuthal and streamwise (axial) directions. The plane of symmetry of the pipe (equatorial mid-plane) is defined by $\theta = \pi/2$, indicated as vertical cut in this paper. The horizontal cut at $\theta = 0$ is also displayed in this schematic view. The curvature parameter κ is defined as R_a/R_c, where R_a is the radius of the pipe cross-section and R_c is the major radius of the torus at the pipe centreline (see Fig. 1a). In general κ distinguishes between mildly (weakly) curved pipes ($\kappa \approx 0.01$) and strongly curved configurations ($\kappa \approx 0.1$).

The incompressible Navier–Stokes equations for the carrier phase read

$$\nabla \cdot \boldsymbol{u} = 0, \tag{1}$$

$$\frac{\partial \boldsymbol{u}}{\partial t} + (\boldsymbol{u} \cdot \nabla)\boldsymbol{u} = -\nabla p + \frac{1}{Re_b}\nabla^2 \boldsymbol{u} \tag{2}$$

Here, $\boldsymbol{u}$ denotes the velocity vector and p the pressure. Re_b indicates the bulk Reynolds number defined as $2R_a u_b/\nu$ where u_b is the bulk velocity, and ν is the fluid kinematic viscosity. The DNSs presented here are performed with the massively parallelised spectral element code `nek5000` [7]. This provides an accuracy similar to spectral methods along with the geometrical flexibility needed by engineering problems. For the fully developed, statistically stationary turbulent flow, no-slip boundary conditions are imposed at the walls while cyclic boundary conditions are applied to the end-sections. As the solution obtained from `nek5000` for the Navier–Stokes equations is in Cartesian coordinates, the streamwise periodicity is guaranteed by an appropriate rotation of the velocity components into the local toroidal coordinate system in order to couple the two ends of the domain. The DNSs are initialised with a laminar Poiseuille profile with superimposed low-amplitude pseudo-random noise acting as three-dimensional perturbations. The simulations are evolved in time until a statistically stationary turbulent state is established (approximately after $200R_a/u_b$). The numerical setup for the carrier phase, the mesh topology and resolution are similar

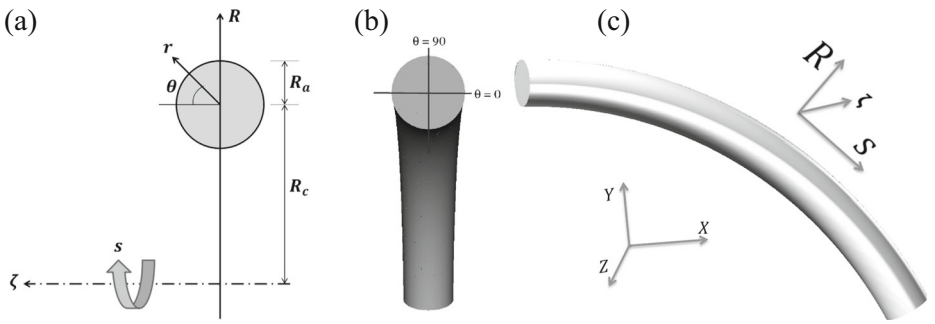

Fig. 1 **a** The schematic front view of the curved configuration with toroidal (R, s, ζ) and in-plane poloidal (r, θ) coordinates. **b** Schematic picture of a general section of a curved pipe, with locations of the cross-sections ($\theta = 0$ as horizontal line, and $\theta = \pi/2$ as vertical/equatorial mid-plane). **c** Side view of the curved pipe geometry and associated coordinate systems, (X, Y, Z) as reference Cartesian coordinates and (R, s, ζ) as attached toroidal coordinate system

to those used by Noorani et al. [16] for the unladen simulations at the highest Reynolds number.

The bulk Reynolds number is fixed to 11700 for both the mildly curved pipe ($\kappa = 0.01$) and the strongly curved pipe ($\kappa = 0.1$), which ensures that the flow remains turbulent in both cases. To compute statistics of the turbulent flow, averages (denoted by $\langle\cdot\rangle$) are taken along the axial/streamwise direction (s), and in time (t). The non-dimensional friction Reynolds number Re_τ, defined as $\overline{u_\tau} R_a/\nu$, is 368 and 410 for the mildly and strongly curved configurations, respectively. The superscript '+' is used to denote quantities expressed in viscous units, normalised with the friction velocity $\overline{u_\tau}$ and ν. The friction velocity is defined as $\sqrt{\overline{\tau_{w,tot}}/\rho_f}$ where ρ_f is the fluid density and $\overline{\tau_{w,tot}}$ denotes the total (vectorial) mean shear stress over the wall. The overbar in $\overline{u_\tau}$ denotes an average along the circumference of the pipe section. Further details on the statistical averaging pertaining the carrier phase via tensor transformations under rotation from Cartesian coordinates to toroidal/poloidal coordinates are given in Noorani et al. [16]. The verification of the method together with the validation of the simulation set-up are also presented there.

The current research concerns low volume fractions of micro-size dilute heavier-than-fluid particles that are assumed to be smaller than the smallest spatial scales of the flow. These can be described as point particles with no force feedback on the flow or inter-particle collisions (i.e. *one-way* coupled). For large enough density ratios ($\rho_p/\rho_f \sim 10^3$; ρ_p being the particle density) the particles are only subjected to the non-linear Stokes drag [18]. Hence each particle evolves according to

$$\frac{\mathrm{d}\boldsymbol{v}_p}{\mathrm{d}t} = \frac{\boldsymbol{u}(\boldsymbol{x}_p, t) - \boldsymbol{v}_p}{St_b} f(Re_p), \tag{3}$$

$$\frac{\mathrm{d}\boldsymbol{x}_p}{\mathrm{d}t} = \boldsymbol{v}_p, \tag{4}$$

where $\boldsymbol{x}_p$ is the particle position, $\boldsymbol{v}_p$ and $\boldsymbol{u}(\boldsymbol{x}_p, t)$ are the particle velocity and the fluid velocity at the particle position, respectively. Equation (3) expresses the particle acceleration ($\boldsymbol{a}_p$) due to the steady-state aerodynamic drag acting on the spherical solid particle in a uniform velocity field. The term $f(Re_p)$ is the *non-linear* correction due to the particle finite Reynolds number, expressed as $(1 + 0.15Re_p^{0.687})$ [24]. The instantaneous particle Reynolds number Re_p is defined as $|\boldsymbol{v}_p - \boldsymbol{u}(\boldsymbol{x}_p, t)|d_p/\nu$. For the current investigation, the effect of gravitational acceleration will be neglected to be able to isolate the effect of the centrifugal force and of the secondary motion of the Dean vortices on the particle behaviour. This does not imply that the gravitational effects are irrelevant in all cases, in particular when considering heavy inertial particles. It is worthwhile to note that in a turbulent flow on a flat-plate boundary layer Sardina et al. [23] have shown that even with large density ratios the effect of gravity becomes negligible when the bulk velocity is large enough.

The particle behaviour is characterised by the Stokes number, the ratio between the particle relaxation time and a flow time scale. Expressing the particle relaxation time $\tau_p = \rho_p d_p^2/(18\rho_f \nu)$ where d_p is the particle diameter, one can determine the bulk Stokes number St_b as the ratio of τ_p to the bulk flow residence time (tu_b/R_a). The viscous time-scale can also be used to analyse the particle response, leading to $St^+ = \tau_p \overline{u_\tau}^2/\nu$.

A spectrally accurate interpolation scheme is applied to evaluate the fluid velocity at the particle position in the flow domain. The order of accuracy of this interpolation is equal to the order of the spectral element method (7 in the current simulations). A classical 3^{rd} order multistep Adams–Bashforth (*AB3*) scheme is applied for the particle tracking time-stepper. The particle interaction with solid walls is treated as purely *elastic* collisions, in other words

the total kinetic energy is conserved in the particle-wall collision process. Similar to the carrier phase, cyclic boundary conditions are used for the dispersed phase in the axial direction. This Lagrangian particle tracking module is verified and validated for a classical particle-laden turbulent channel flow against Sardina et al. [22]. The implementation, validation and verification of the particle tracking module are reported by Noorani [15].

A total of seven particle populations corresponding to different St_b, are simulated in the current study. The density ratio is fixed to $\rho_p/\rho_f = 1000$ for all populations. The radius of the particles is changed to obtain the different bulk Stokes number. Similar to laboratory experiments, the St_b of each population is kept constant when varying the curvature κ, which corresponds to fixing the physical particles (i.e. fixing the particle density and radius) when the curvature parameter varies. Table 1 defines the various particle populations and their corresponding parameters. The **Stp100** population represents the limit of the ballistic behaviour of heavy inertial particles while the **Stp0** particles are tracers and their Eulerian statistics reproduce the flow field averages.

The particles are introduced into the fully developed turbulent velocity field with a uniform random distribution in the radial r, azimuthal θ and axial s directions; their initial velocity is set equal to the local flow velocity. It can be shown that the dispersed phase reaches the statistically steady state at about $1500R_a/u_b$ for all particle populations and curvatures investigated. The simulations are then continued for $1500R_a/u_b$ to collect enough samples for the statistical analysis.

Eulerian statistics are obtained from the Lagrangian particle data as in **bpPart15**. As a short summary, for quantities dependent on the radial direction, the pipe domain is divided into wall-parallel axisymmetric slabs. These slabs are distributed non-uniformly according to the function:

$$r = R_a(1 - (\sinh \gamma \eta)/(\sinh \gamma))$$

with $\gamma = 3$ being the stretching factor. The variable η indicates an uniformly spaced grid. The binning is thus more resolved near the wall than in the middle of the pipe. An additional grid is also generated in the azimuthal direction to build a mesh in the in-plane poloidal space. The particles are binned into these cells to obtain the Eulerian maps presented below. A total of 2821 cells are used for the 2D representation of the statistics: $N_\theta = 91$ and $N_r = 39$, with $\gamma = 2$; N_θ and N_r being the number of cells in the azimuthal and wall-normal directions respectively. Similarly, the statistical analysis in the horizontal and equatorial mid-plane of the curved pipes is carried out with 100 wall-parallel slabs with stretching

Table 1 Definition of the particle population under investigation

Case	d_p/R_a	$r_{p(\kappa=0.00,\ Re_\tau=360)}^{+}$	St_b	$St_{(\kappa=0.01)}^{+}$	$St_{(\kappa=0.1)}^{+}$
Stp0	n/a	n/a	0.0	0.0	0.0
Stp1	3.727×10^{-4}	0.0671	0.0451	1.0503	1.3020
Stp5	8.333×10^{-4}	0.1500	0.2257	5.2516	6.5095
Stp10	1.179×10^{-3}	0.2121	0.4514	10.503	13.020
Stp25	1.863×10^{-3}	0.3354	1.1284	26.258	32.547
Stp50	2.635×10^{-3}	0.4744	2.2569	52.516	65.095
Stp100	3.727×10^{-3}	0.6708	4.5139	105.03	130.20

The number of particles per population N_p is 128 000. The density ratio ρ_p/ρ_f is fixed to 1000 for all populations. The bulk Stokes number St_b and particle diameter d_p/R_a of each population is fixed while the curvature is varied in each flow configuration ($\kappa = 0.01$, and 0.1)

$\gamma = 2$ in the distribution function above and a constant cell-width of 20 viscous units. The convergence of the particle statistics is shown in **bpPart15**.

3 Results

A detailed analysis of the turbulent curved pipe flows at the same Reynolds number and curvatures investigated here can be found in [16]. A brief overview of the key flow features in these configurations is also presented in **bpPart15** and it will therefore not be repeated here.

3.1 Particle concentration

The particle accumulation in strongly and mildly curved pipes is investigated using the particle concentration C defined as the number of particles per unit volume normalised with the mean (bulk) concentration at uniform distribution. The map of the concentration is determined by the combination of multiple effects such as geometry induced centrifugal acceleration, Dean cell centrifugation, turbulent dispersion and particle-wall collisions. Figure 2a, b displays the normalised mean particle concentration maps for the mildly curved pipe and particle populations **Stp10** and **Stp100**. The values are shown in logarithmic scale.

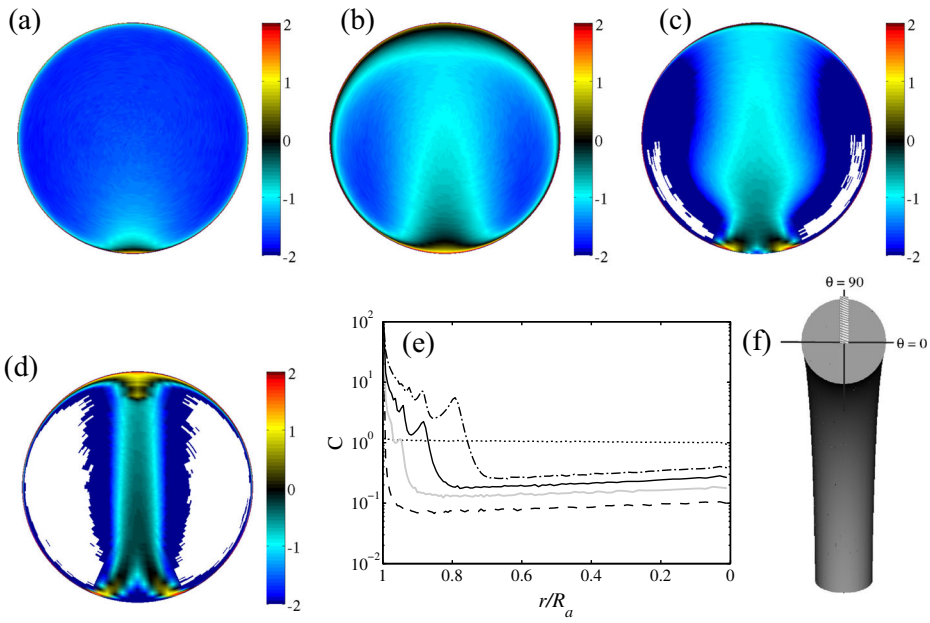

Fig. 2 Mean particle concentration normalised with that of an uniform distribution, in logarithmic scale ($\log_{10}(C)$), in the mildly curved pipe ($\kappa = 0.01$) for **a**: **Stp10** , and **b**: **Stp100**. Same in the strongly curved pipe ($\kappa = 0.1$) for **c**: **Stp10**, and **d**: **Stp100**. Note that the cells in which no particles enter during a simulation interval of $1500R_a/u_b$ (the statistical time frame) are illustrated in *white*. The equatorial mid-plane (vertical cut) of the strongly curved pipe ($\kappa = 0.1$) is shown in **e** to visualise the near-wall reflection layers. The outer bend is located at $r/R_a = 1$ and the pipe centre is at $r/R_a = 0$. ..... **Stp0**, - - - - **Stp5**, ——— **Stp25**, ——— **Stp50**, and —·— **Stp100**. **f** the shaded region on the schematic pipe is the station in which the data in **e** are acquired

It becomes clear that although particles in curved configurations still largely accumulate in the near-wall region, the mean particle concentration is strongly non-homogeneous even at the smaller curvature examined here. The **Stp10** particles mainly aggregate near the inner bend stagnation point while the majority of the pipe section is almost depleted of the particulate phase. When further increasing the particle inertia, the particle accumulation reflects more clearly the secondary motion and we observe a plume of higher concentration rising from the inner bend towards the outer bend along the plane of symmetry of the pipe. This creates a region of higher concentration near the outer bend. The core of the mean Dean vortices of the carrier phase is a stable highly-vortical region and remains at the lowest concentration for the largest (heaviest) particles, as expected.

The mean particle concentration is illustrated in Fig. 2c, d for the strongly curved pipe. Comparing with the mildly curved pipe, we see a fanning effect appearing because of the higher turbulent level in the bulge region (c.f. Fig. 9 in [16]). In particular, the concentration decreases near the core of the mean Dean vortices as much as there are areas where we do not find any particles during the averaging time of $1500R_a/u_b$. Hereinafter these cells are illustrated in *white*. In this configuration ($\kappa = 0.1$), the root of the particle plume rising from the inner bend is split into two parts that are located farther from each other with increasing the particle inertia and the area depleted from the particle grows substantially. The particles with highest Stokes number follow ballistic trajectories to create a narrow confluence of the solid phase along the equatorial mid-plane. This leads to wall-particle collisions at the outer bend, which in turn generate multiple reflection layers adjacent to the outer bend stagnation point.

These reflection layers –readily seen as peaks in the concentration maps pertaining the largest Stokes numbers (Fig. 2e)– are interesting features of the particulate phase in the presence of strong secondary motions. They appear only for populations with **Stp5** or more and in the case with $\kappa = 0.1$ when the secondary motion is large enough. These can be explained by the intense wall rebounds at the outer bend. The incoming speed determines how far the particle reaches inside the domain after the collision, and this increases for heavier particles. This phenomenon, already observed by Huang & Durbin [10] in an S-shaped channel, is explained in their study with the aid of a simplified model.

3.2 Particle velocities

We display in Fig. 3 the mean streamwise particle velocity, $\langle v_{s_p} \rangle$, and the magnitude of the in-plane velocities, $\sqrt{(}\langle v_{r_p} \rangle^2 + \langle v_{\theta_p} \rangle^2)$, in the cross-section for the case with $\kappa = 0.01$, where the velocities are normalised with the bulk flow (u_b). Note that the data at the pipe centreline are removed due to the singularity of the poloidal components. Although the mean particle velocities are almost identical to the flow velocities for **Stp1** (c.f. Fig. 7 in [16]), for the other populations the streamwise velocity is slightly slower than that of the fluid at the outer layer region ($(1 - r/R_a)^+ \gtrsim 50$). A quantitative analysis of this reduction is offered in Fig. 4a, b in the vertical and horizontal cuts. Increasing the importance of the particle inertia, the position of the maximum of $\langle v_{s_p} \rangle$ moves towards the outer bend. With the exception of the near-wall region, the magnitude of the streamwise component decreases by 5 % near the outer bend ($r/R_a \approx 0.75$) and 10 % near the inner bend ($r/R_a \approx -0.75$) for the heaviest particles. This reduction in the streamwise velocity component of the inertial particles is already addressed in the literature for canonical wall-bounded turbulent particle-laden flows [4, 14, 20] and linked to the preferential accumulation of inertial particles in low-speed regions.

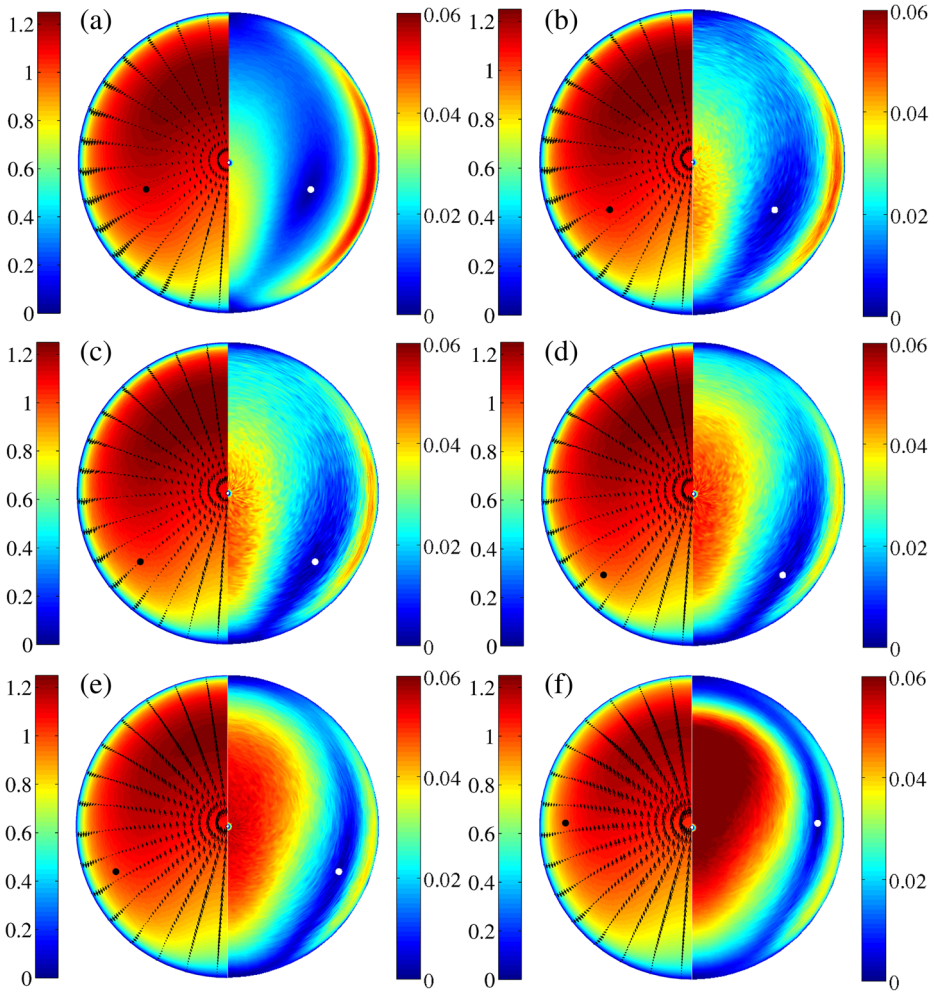

Fig. 3 (*Left*) Pseudocolours of the streamwise component of the mean particle velocity in the mildly curved pipe with the vectors for the in-plane motion. (*Right*) Pseudocolours of the magnitude of mean in-plane velocities of the particulate phase in the same configuration. Black and white dots indicate the core of the mean Dean vortices associated with the particulate phase data. **a Stp1**, **b Stp5**, **c Stp10**, **d Stp25**, **e Stp50**, **f Stp100**

Interestingly, the particle mean in-plane velocities deviate greatly from that of the fluid flow. From the right-half of the 2D plots in Fig. 3 it is clear that the secondary motion of the heavier particles is slower on the side-wall boundary layers (SWBL). On the contrary, their in-plane velocity increases significantly in the pipe core, particularly in the vicinity of the equatorial midplane. The radial velocity, the only non-zero component of the in-plane motion in the plane of symmetry of the pipe section, is shown in Fig. 4c for the mildly curved pipe. For visualisation purposes, to maintain the continuity of the $\langle v_{r_p} \rangle$ plots in the equatorial midplane, the values in the inner-bend portion of the plots ($r/R_a < 0$) are multiplied by a -1. From the Fig. 4c it is clear that increasing the population Stokes number,

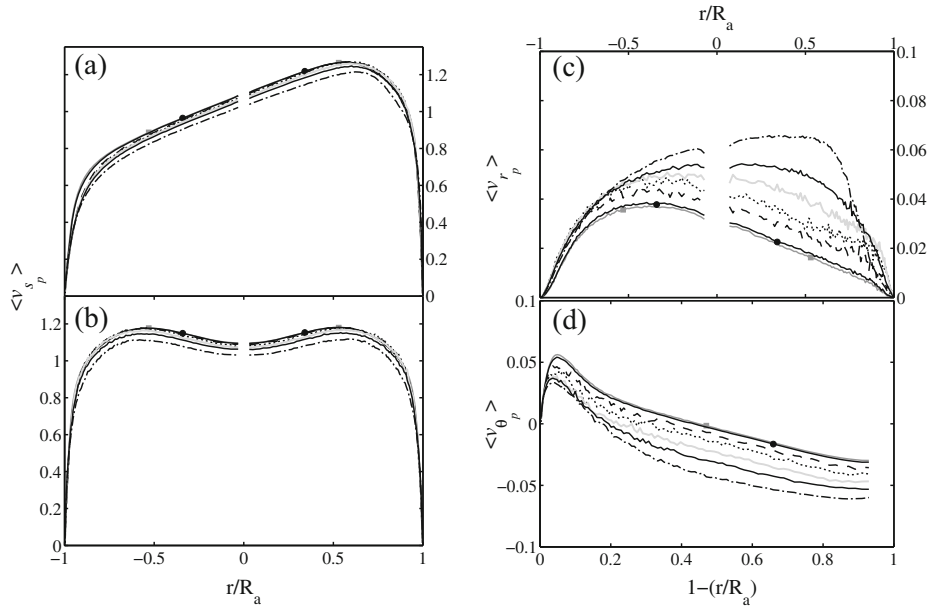

Fig. 4 Mean particle streamwise velocity at **a** the equatorial midplane of the pipe section (vertical cut) and **b** in the horizontal cut of the pipe section. **c** Mean particle radial velocity at the equatorial midplane of the pipe section (vertical cut). The inner and the outer boundaries are at $r/R_a = -1$ and $r/R_a = +1$. **d** Particle azimuthal velocity at the horizontal cut of the pipe section. Here $(1 - r/R_a) = 0$ indicates the position of the side-wall. — ■ — **Stp0**, — ● — **Stp1**, - - - - **Stp5**, ... **Stp10**, **Stp25**, ——— **Stp50**, — · — **Stp100**

the particles become much faster than the fluid flow in the radial direction and the maximum of $\langle v_{r_p} \rangle$, located near the inner bend for tracers and low-inertia particles, becomes twice as large and moves towards the outer bend. This increases the possibility of wall-particle collisions at the outer bend. The mean azimuthal component of the velocity $\langle v_{\theta_p} \rangle$ at the horizontal cut of the pipe section ($\kappa = 0.01$) is displayed in Fig. 4d to reveal, in particular, that the near-wall maximum of $\langle v_{\theta_p} \rangle$ is almost half of that of the fluid flow for **Stp100**.

Next, we examine the particulate phase as an Eulerian field to determine the core of the mean Dean vortices associated to the particle motions from the in-plane velocity components (see Fig. 3). For the mildly curved pipe, increasing the Stokes number of the population, the vortex core is squeezed further towards the wall as if the strength of the embedded mean vortical structure is increased. This could have important implications in the case of higher particle mass loading when the two phases are fully coupled. One could in fact expect that, in those cases, the solid phase may significantly alter the secondary motion of the fluid phase.

The mean particle velocities are illustrated in Figs. 5 and 6 for the strongly curved pipe. The figures show that the above mentioned trends are further amplified by an increase in the magnitude of the flow secondary motions. The further reduction of $\langle v_{s_p} \rangle$ with increasing particle Stokes number is clear in Figs. 5 and 6. Except for very close to the wall, this reduction is around 10 % and 20 % near the inner and the outer bend, respectively, for the **Stp100** particles. Note that the statistics are less accurate in the regions of smallest

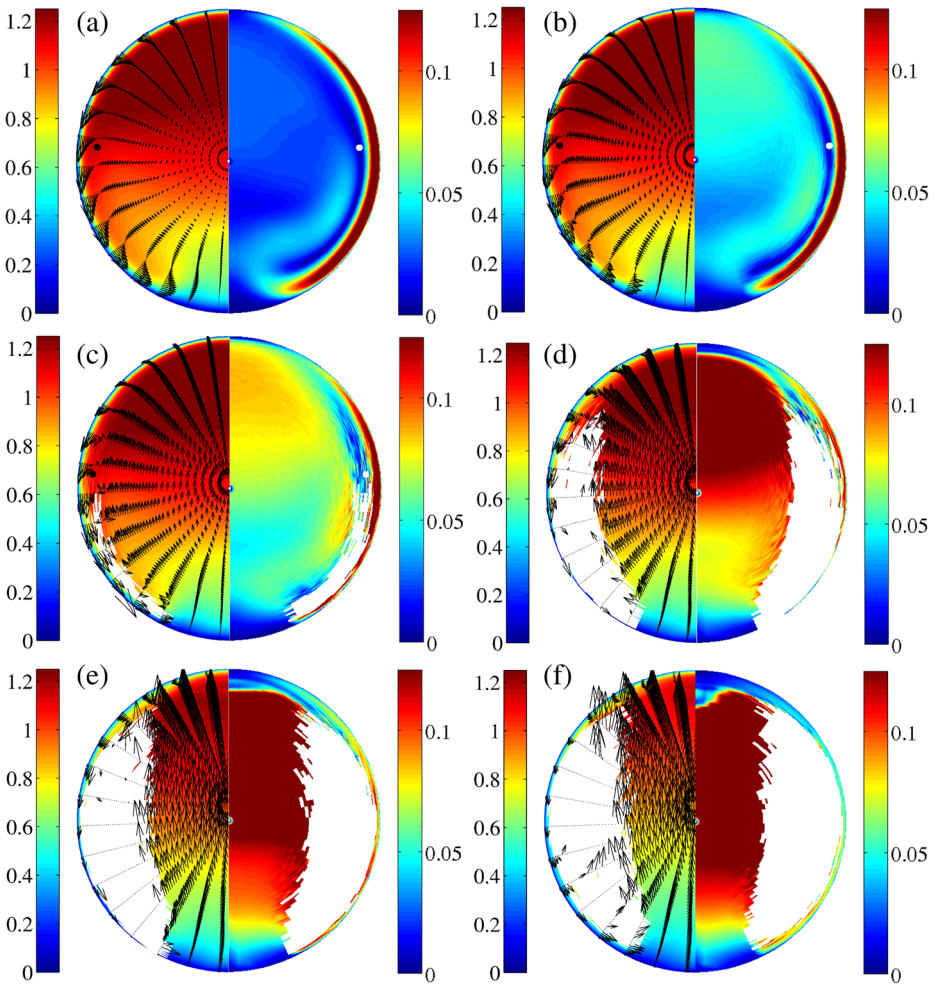

Fig. 5 Same as Fig. 3 but for the strongly curved configuration ($\kappa = 0.1$)

concentration and near areas where no particle data are available (depleted regions that are shown in *white* in Fig. 2).

The magnitude of the in-plane particle motion in the strongly curved pipe changes with St as shown by the 2D plots in Fig. 5. The effect of the particle–wall collisions is clear for **Stp50** and **Stp100** near the outer bend where inertia prevents particles from following the flow streamlines. This specular reflections change the direction of the radial velocity at the outer bend and expel particles from the near-wall region. Consequently, the magnitude of the in-plane velocities is drastically reduced in the vicinity of the outer bend wall for these populations. The effect of the reflection layers is more obvious in Fig. 6c. The consecutive peaks of $\langle v_{r_p} \rangle$ near the outer bend show how the radial velocity cancels due to the superposition of reflected particles with negative radial velocity. The position of the troughs in $\langle v_{r_p} \rangle$ at the outer bend coincides exactly with the crests of the outer-bend oscillations in the concentration plot in Fig. 2. Similarly to the mildly curved pipe, the maximum of $\langle v_{r_p} \rangle$ moves

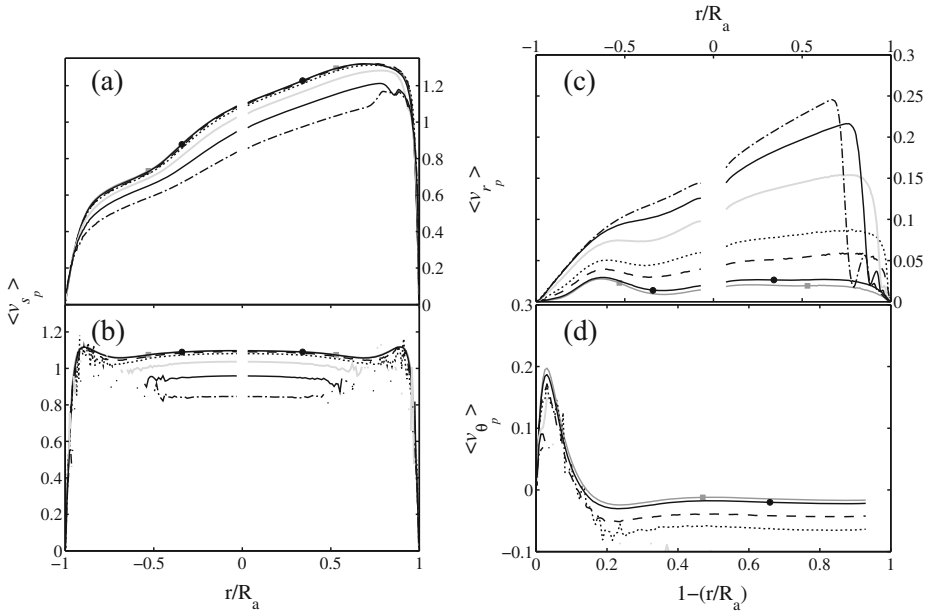

Fig. 6 Same as Fig. 4 but for the strongly curved configuration ($\kappa = 0.1$)

towards the outer bend when increasing the particle Stokes number, although this is more evident here as it occurs for all populations except the **Stp1**. The general trend from the horizontal cut of $\langle v_{\theta_p} \rangle$ suggests that the behaviour is similar to what is observed in the mildly curve pipe, although a quantitative analysis is not amenable due to the lack of particle data in the depleted regions .

Unlike the radial velocity of the particles that is reversed after the wall collision, the streamwise component remains the same; nevertheless, the peaks of $\langle v_{s_p} \rangle$ near the outer bend are also due to the reflection layers (see Fig. 6a) and the transport of low-momentum particles from regions on the sides.

Finally, the core of the Dean vortices associated with the particulate phase are also squeezed farther towards the wall with enhancing the particle inertia when $\kappa = 0.1$. Note again that it is difficult to pinpoint the vortex core at high St due to the lack of statistical data in this region.

3.3 Particle velocity fluctuations

The influence of the inertia on the particle velocity fluctuations is displayed for both configurations in Fig. 7 where we report the turbulent kinetic energy (TKE) of the particulate phase in the cross-section. The TKE is defined as $k = \langle v'_{i_p} v'_{i_p} \rangle / 2$, with primes indicating the fluctuating velocity. In the mildly curved pipe, the fluctuation energy k decreases when increasing the particle inertia for the largest part of the pipe section. This is similar to what previously reported in turbulent straight channels and pipes [19, 20], and explained by the particle inertia that filters the fastest turbulent motions.

The same trend is observed in the strongly curved pipe; the main difference is the occurrence of large values of k near the outer bend when increasing St, in the regions where the

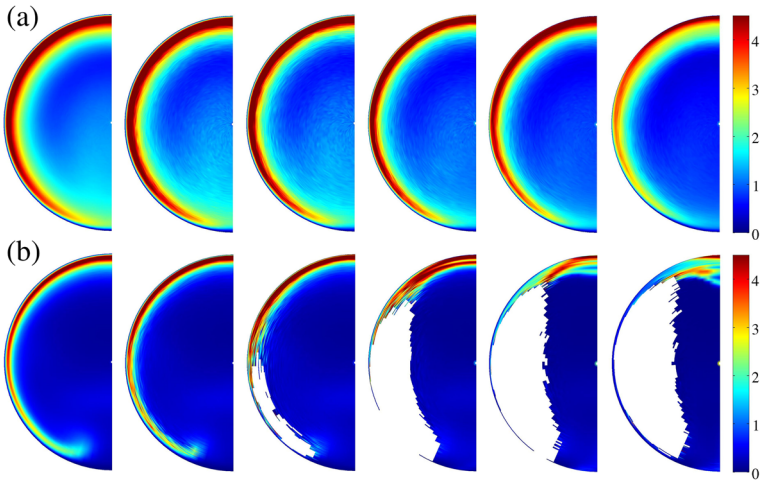

Fig. 7 Pseudocolours of turbulent kinetic energy of the particulate phase normalised with the friction velocity $\overline{u_\tau}^2$ of the fluid flow. **a** curved pipe with $\kappa = 0.01$; and **b** curved pipe with $\kappa = 0.1$. *From left to right:* **Stp1**, **Stp5**, **Stp10**, **Stp25**, **Stp50**, **Stp100**

reflection layers form. This is due to fast particles penetrating the low velocity regions after the reflections. Multiple peaks of turbulent kinetic energy are therefore found in the outer bend, located at the edge of the reflection layers where there is a large gradient in the radial velocity. As observed for $\langle v_{r_p} \rangle$, the position of the minima of the turbulent kinetic energy in the equatorial midplane coincides with the crests of the concentration (see Fig. 2).

To provide further details on the individual components of the velocity fluctuations, the root-mean-squared (r.m.s) of the streamwise velocity is shown in Fig. 8a, b in the equatorial mid-plane of the pipe. For both curvatures under investigation, the streamwise particle velocity fluctuations, v_{s,rms_p}, are slightly larger than those of the flow in the vicinity of the outer bend, as expected from previous studies on straight particle-laden turbulent wall-bounded flows. As explained among others by Portela et al. [20] considering the mean fluid-velocity gradient, this is due to the wall-normal motions between regions of high and low $\langle u_s \rangle$. In this case, the mean radial flow towards the outer bend further enhances this effect. For both curvatures, the maximum of v_{s,rms_p} moves towards the outer-bend wall for the populations of largest Stokes number.

The mean radial flow is not directed towards the wall at the inner bend, but towards the pipe centre. Hence, the peak of v_{s,rms_p} is reducing with the Stokes number, St. This is more clearly seen in the bulge region ($r/R_s = -0.4$) of the strongly curved configuration (c.f. Figs. 9, 13 in [16]) where particles with large Stokes numbers (and thus long enough *memory*) are transported by the secondary motion from the quiescent region in the inner bend to this bulge region. The effect is larger for heavier particles and the peak is much less evident for the population **Stp100**. The noisy peaks adjacent to the inner part of the wall in the simulation with $\kappa = 0.1$ are caused by the rare heavy particles that have not followed the flow in-plane streamlines due to their inertia. The very high flatness of the fluctuations occurring in this partially relaminarised region and the very dilute concentration explain the noisiness in the profile. Correspondingly, the peak adjacent to the inner bend becomes larger with increasing inertia.

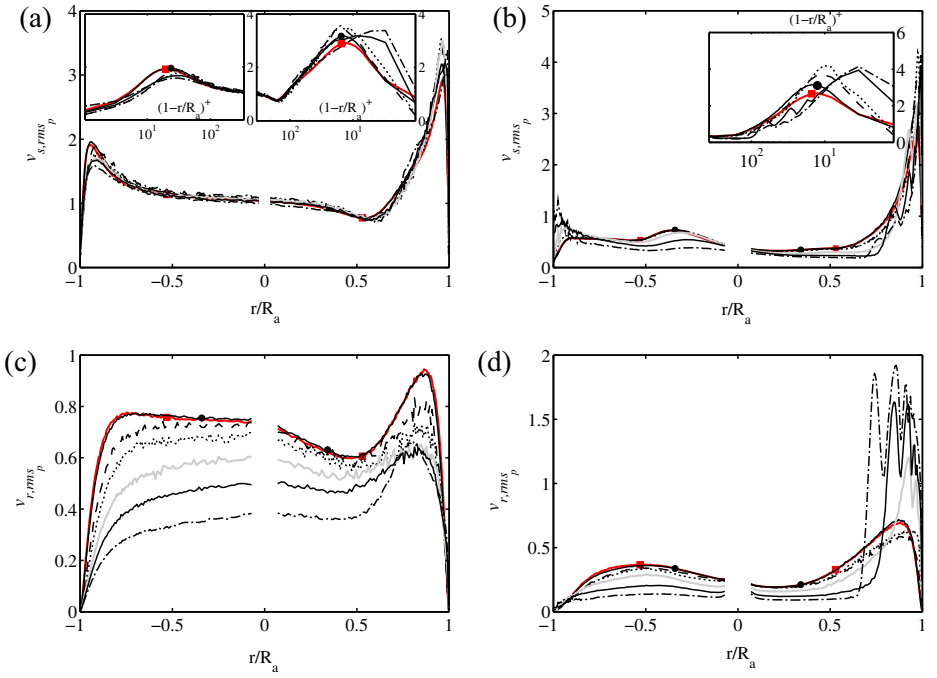

Fig. 8 Particle streamwise r.m.s velocity normalised with the flow mean friction velocity in a vertical cut of **a** mildly curved pipe, and **b** strongly curved pipe. Wall-normal r.m.s velocity normalised with the flow friction velocity in vertical cut of **c** mildly curved pipe, and **d** strongly curved pipe. The inner and the outer bend are at $r/R_a = -1$ and $r/R_a = +1$ respectively. The wall distance is shown in inner units in the insets. **Stp0**, **Stp1**, **Stp5**, **Stp10**, **Stp25**, **Stp50**, **Stp100**

Excluding the region close to the outer bend where heavy particles experience reflections at the wall, the radial velocity fluctuations are lower than those of the fluid phase. Unlike straight pipe and channel flows, there exist a radial (wall-normal) mean particle velocity in bent configurations and hence, the mean drag force due to the centrifugal forces is balanced by the turbophoretic drift towards the wall at the inner bend. The existence of the flat peaks near the inner bend provide some evidence for that.

3.4 Dispersed phase fluxes

To investigate the particle transport in toroidal pipes, the dispersed-phase fluxes are analysed in the pipe section and horizontal cuts. The particle flux J is defined as particle number density per unit volume multiplied by the corresponding velocities. We recall that the particle transient behaviour has been investigated in **bpPart15**. We note that shortly after injecting the solid particles in the fully developed turbulent flow, quasi-periodic oscillations of the near-wall concentration are observed for various populations (c.f. Fig. 9 in [17]). This is linked to the action of the secondary motion on the particles in the initial stage of the simulations. Due to their inertia, the majority of the particles initially moves towards the outer bend under the influence of the centrifugal forces. These particles then move along the side walls, a process modulated by the flow turbulence. The particle motion reaches a statistical steady state about $1500 R_a/u_b$ time units after their injection. A schematic view of the main

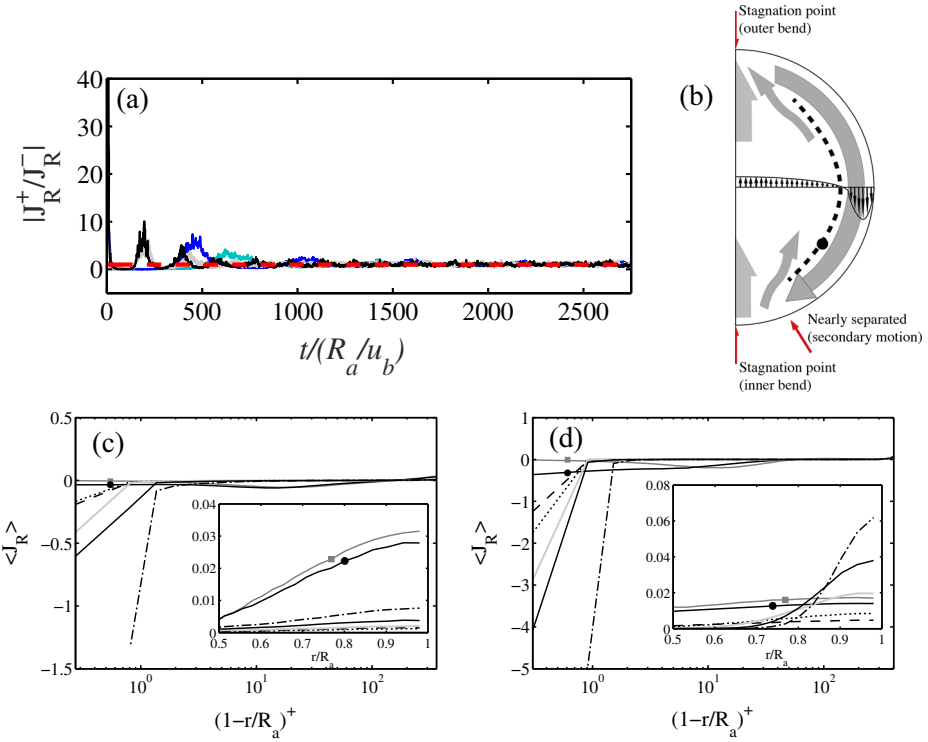

Fig. 9 **a** Time evolution of the ratio of outward and inward instantaneous particle flux in the radial direction across the horizontal cut of the strongly curved pipe. $t = 0$ denotes the particle injection time. **Stp5**, **Stp10**, **Stp50**, **Stp100**, equilibrium state $|J_R^+/J_R^-| = 1$. **b** Schematic illustration of the secondary motion in a typical bent pipe. The side-wall boundary layer and the lifted secondary flow from the inner bend are sketched with dark and light gray respectively. The filled circle and the dashed line display a typical Dean-vortex and mixing layer core. A sketch of the velocity vectors of the secondary motion in the horizontal cut is displayed also in the figure. **c**: Mean particle flux in the torus radial direction $\langle J_R \rangle$ in the horizontal cut of the mildly curved pipe and **d** strongly curved pipe, normalised with the total streamwise flux of passive tracers. Same symbols as Fig. 4

features of the carrier phase secondary motion driving this process in a bent pipe is sketched in Fig. 9b.

Figure 9a displays the time variation of the ratio of the particle flux towards the outer bend (J_R^+) to the particle flux towards the inner bend (J_R^-). These are computed from the time of injection and recorded across the horizontal cut of the strongly curved pipe. At equilibrium, the two fluxes are equal, i.e. $|J_R^+/J_R^-| = 1$, as indicated by the dashed line in the figure. Still 200 convective time units after the injection time, the flux towards the outer bend is almost an order of magnitude larger than the one towards the inner bend for the heaviest population. Nonetheless, the lighter populations (e.g. **Stp5** particles) need longer times to reach equilibrium. As already mentioned, the statistically steady state is reached around $t = 1500 R_a/u_b$.

Recalling that, on the one hand, the concentration on the side-wall of these curved configurations is two to four orders of magnitude larger than that at the pipe core, and that, on the other hand, the in-plane velocity is larger in the pipe-core than on the side walls. The equilibrium particle state is only possible via a large flux from the side walls. Figures 9c,

d therefore illustrate the particle flux in the torus radial direction (R) in a horizontal cut of the pipe section. This is normalised with the total streamwise particle flux per pipe section $\langle J_{s,tot} \rangle$ pertaining to passive tracers (i.e. **Stp0**). Here, negative $\langle J_R \rangle$ indicates a flux towards the inner bend whereas positive values indicate particle flux towards the outer bend. For both curvatures, the fluxes towards the inner bend are significantly larger than those towards the outer bend, and for almost all particle populations this transport occurs in the viscous sublayer. Without exceptions, the magnitude of the flux along the side walls increases with particle inertia.

It can be seen in the insets of Fig. 9c, d that the outwards flux decreases near the centreline of the mildly curved pipe when increasing St; in the strongly curved configuration, however, it first decreases and then increases sharply with the population Stokes number. This flux towards the outer bend may be smaller than the in-plane near-wall flux but it has a large impact on the mean streamwise particle flux $\langle J_{s,tot} \rangle$. This quantity is reported in Fig. 10a for pipes with different curvature. The data are also compared to those from a straight pipe in **bpPart15**. Analysis of these results reveals that, when increasing the particle inertia, the axial particle flux first decreases drastically and then slowly recovers, independent of the curvature. More importantly, the flux of the inertial particles through the pipe section significantly increases when increasing the bend curvature, except for the case **Stp1**. This is illustrated in Fig. 10b where we report the ratio of the axial particle flux in the bent pipe to that of the straight configuration for various Stokes numbers. It is apparent that the largest gain is attained by the **Stp10** particles. These particles are more sensitive to curvature effects.

3.5 Acceleration statistics

An adequate description of the acceleration statistics is essential to model the solid particulate dispersion in wall-bounded turbulent flows [27]. Recent experimental and numerical studies address the near-wall behaviour of the particle acceleration as well as its variance [8, 13, 29, 31]. In the context of homogeneous isotropic turbulence (HIT) it is known that as the particle inertia increases the r.m.s of the acceleration decreases [1, 3]. According to Bec et al. [3] the two concurrent mechanisms responsible for this behaviour are the preferential

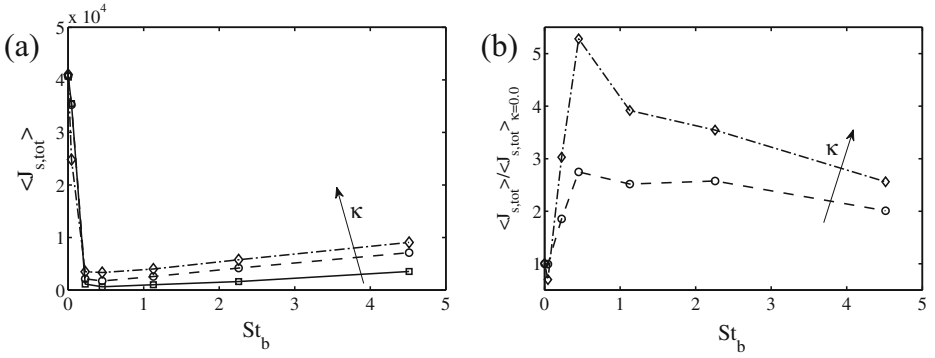

Fig. 10 **a** Mean streamwise particle flux averaged across the pipe section $\langle J_{s,tot} \rangle$ for different Stokes number and different configurations. **b** Ratio of the mean axial particle flux in the bent pipe to that of the straight pipe. —□— $\kappa = 0.00$; —○— $\kappa = 0.01$; —◇— $\kappa = 0.10$

concentration and the filtering of the high-frequency turbulent fluctuations. While the latter is more effective for larger particle inertia, the former effect (particle centrifugation out of intense vortices) is more important at lower St. This can influence the particle acceleration variance by increasing the residence time of the particle in the high-strain (low-vorticity) regions [6].

The influence of the Stokes number on the mean streamwise acceleration, $\langle a_{s_p} \rangle$, is illustrated in Fig. 11. Except in the near-wall regions, $\langle a_{s_p} \rangle$ is almost uniform across the pipe section and assumes similar values for the various populations. The largest streamwise acceleration appears at the inner bend and its value decreases towards the outer bend when increasing the particle inertia. Figure 12a offers a quantitative comparison of the particle acceleration $\langle a_{s_p} \rangle$ between different populations in the plane of symmetry of the pipe. Moving outwards, the mean streamwise acceleration of the solid phase first increases and then decreases to reach a minimum near the wall at the outer bend, this effect being more pronounced for the population of lowest Stokes number. This is similar to the behaviour observed in canonical channel flows [31] where this deceleration is explained in terms of the dissipative nature of the Stokes drag. Further, we note that the **Stp1** particles have a maximum streamwise deceleration near the inner-bend wall for $\kappa = 0.01$; when increasing the Stokes number, $\langle a_{s_p} \rangle$ becomes positive and reaches a maximum for the **Stp10** population. Further increasing the particle inertia, the maximum reduces although its value remains positive. This variation is due to the anti-alignment of the flow shear and centrifugal forces.

The behaviour of the mean radial component of the particle acceleration, $\langle a_{r_p} \rangle$, reported in Fig. 12c, is similar to that of the streamwise component in the outer bend of the mildly curved pipe although its values almost halved. In the inner bend, however, $\langle a_{r_p} \rangle$ has a positive peak close to the wall whose magnitude decreases with increasing particle Stokes number. The mean streamwise acceleration in the pipe core and the deceleration near the outer bend are more pronounced in the strongly curved configuration. The streamwise acceleration $\langle a_{s_p} \rangle$ increases near the pipe centreline with increasing St (Fig. 11b) for the case with $\kappa = 0.1$. Near the outer-bend wall, the maximum particle decelerations appears for the

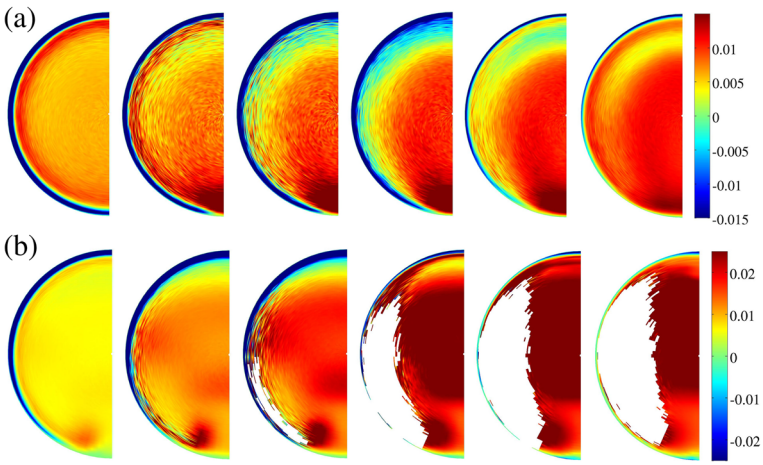

Fig. 11 Pseudocolours of mean streamwise particle acceleration normalised with $\overline{u_\tau}^3/\nu$ of the fluid flow in **a** curved pipe with $\kappa = 0.01$ and **b** in strongly curved pipe ($\kappa = 0.1$). *From left to right:* **Stp1**, **Stp5**, **Stp10**, **Stp25**, **Stp50**, **Stp100**

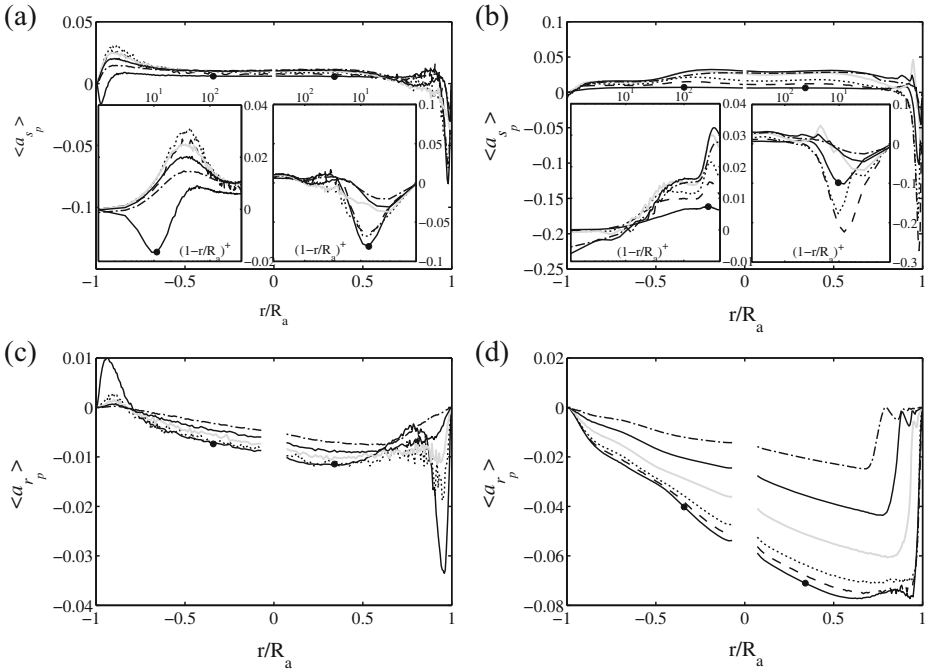

Fig. 12 Mean streamwise particle acceleration $\langle a_{s_p} \rangle$ in the vertical cut of **a** mildly curved pipe and **b** strongly curved pipe normalised with $\overline{u_\tau}^3/\nu$ of the fluid flow. Mean radial particle acceleration $\langle a_{r_p} \rangle$ in **c** mildly curved pipe and **d** strongly curved pipe, also normalised with $\overline{u_\tau}^3/\nu$. Same symbols as Fig. 4. The inner and the outer bend are at $r/R_a = -1$ and $r/R_a = +1$, respectively. The distances scaled in inner units are shown in the insets

particles with **Stp5** (Fig. 12b). Approaching the inner-bend wall, the streamwise acceleration decreases such that $\langle a_{s_p} \rangle$ becomes more uniform among the different populations; very close to the inner-bend wall only the heaviest particles decelerate.

The position of the reflection layers can also be seen in the vertical cut displaying $\langle a_{r_p} \rangle$ in the strongly curved configuration (Fig. 12d). The negative acceleration increases for all the populations from the inner to the outer bend, the effect being more pronounced for the particles of lowest inertia; indeed, the profile reaches a minimum half-way through the outer bend for the **Stp1** particles. In comparison to the mild curvature case, $\langle a_{r_p} \rangle$ is almost three times larger in this configuration for the same populations.

Unlike HIT, the experimental results of Gerashchenko et al. [8] and the numerical simulation of Zamansky et al. [31] suggest that in particle-laden wall-bounded turbulent flows the near-wall peak of the streamwise component of the acceleration variance first increases with the Stokes number, up to $St^+ \sim 5$, and then decreases. These authors also observed that the wall-normal acceleration r.m.s decreases when increasing St, and for all populations its value remains lower in magnitude compared to the streamwise component.

The streamwise, a_{s,rms_p}, and wall-normal, a_{r,rms_p}, components of the acceleration variance are displayed in the plane of symmetry of the curved pipes in Fig. 13. The data indicate the same behaviour observed in straight channels [31]. Excluding the inactive partially relaminarised flow at the inner bend of the strongly curved pipe, the **Stp5** particles display the maximum of a_{s,rms_p}, which is located near the wall. Moreover, a_{s,rms_p} is weak in the

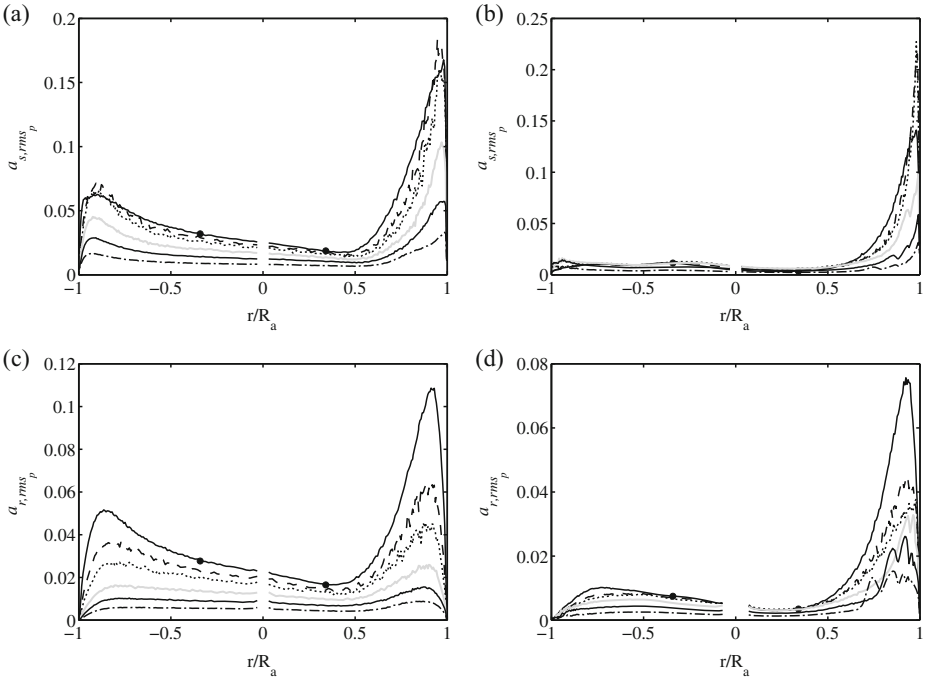

Fig. 13 Streamwise particle acceleration r.m.s a_{s,rms_p} in the vertical cut of **a** mildly curved pipe and **b** strongly curved pipe normalised with $\overline{u_\tau}^3/\nu$ of the fluid flow. Radial (wall-normal) particle acceleration r.m.s, a_{r,rms_p}, for **c** mildly curved pipe and **d** strongly curved pipe also normalised with $\overline{u_\tau}^3/\nu$. Same symbols as Fig. 4. The inner and the outer bend are located at $r/R_a = -1$ and $r/R_a = +1$, respectively

strongly curved pipe (Fig. 13b) and the peaks near the outer bend are larger for the populations of lower Stokes number (see Fig. 13a). The sequence of minima and maxima due to the specular reflection of the heavy particle in the high curvature configuration is apparent in both a_{s,rms_p} and a_{r,rms_p}. For all populations, the wall-normal acceleration r.m.s is smaller in the strongly curved pipe than in the case with $\kappa = 0.01$.

4 Conclusions

We present first and second order moments of the velocity and acceleration of small rigid particles transported in turbulent curved pipe flows with weak and strong curvature. The work extends the analysis of the particle distribution by Noorani et al. [17]. The simulations employ an efficient spectral element method for the fluid flow one-way coupled with a Lagrangian tracking algorithm for the solid phase.

The curved pipe is an example where cross-stream secondary motions are induced by the geometry and centrifugal forces. The aim of this study is therefore to understand the role of the cross-stream secondary motions (Dean vortices) on the particle dynamics. We identify the mean Dean vortices associated to the motion of the particles and show that these are moved towards the side-walls and, interestingly, are more intense than those of the mean flow.

Similar to canonical particulate turbulent channel and pipe flows, the mean streamwise velocity of the particles is lower than that of the fluid flow, and it further decreases enhancing the particle inertia. The effect of the Stokes number is found to be more pronounced on the in-plane motion of the particles, which move inwards along the pipe side walls and then rise quickly across the pipe core. This secondary motion causes intense wall-particle collisions of the heaviest populations and in the strongly curved configuration at the outer bend which in turn induce reflection layers as previously discussed for the concentration map in the companion article by Noorani et al. [17]. Such reflectional mixing generates fluctuations of the particle radial velocity higher than in the flow. Elsewhere in the pipe, the flow velocity fluctuations are larger than those of the particles due to the inertial filtering by the solid phase.

Turbophoresis and particle velocities are combined examining the particle flux in the streamwise and transverse directions of the pipe section. The particle flux is significantly larger along the side walls in the viscous sublayer of the fluid flow than near the pipe centreline. This side-wall in-plane flux increases with the particle Stokes number. The weak flux from the inner to the outer bend determines an increased streamwise particle flux: for the **Stp10** population in the strongly curved pipe, for instance, the mean axial particle flux is five times that in the straight pipe.

Finally, the streamwise and wall-normal acceleration and their variance are examined. The streamwise component statistics are similar to those of canonical wall-bounded particle-laden flows at the outer bend of both the strongly and weakly curved pipes, whereas differences are observed on the inner side, especially in the case with strong curvature where the flow is highly intermittent. The wall-normal acceleration is largely affected by the mean secondary motion.

References

1. Ayyalasomayajula, S., Gylfason, A., Collins, L., Bodenschatz, E., Warhaft, Z.: Lagrangian measurements of inertial particle accelerations in grid generated wind tunnel turbulence. Phys. Rev. Lett. **97**(14), 144,507 (2006)
2. Balachandar, S., Eaton, J.K.: Turbulent dispersed multiphase flow. Annu. Rev. Fluid Mech. **42**, 111–133 (2010)
3. Bec, J., Biferale, L., Boffetta, G., Celani, A., Cencini, M., Lanotte, A., Musacchio, S., Toschi, F.: Acceleration statistics of heavy particles in turbulence. J. Fluid Mech. **550**, 349–358 (2006)
4. Bernardini, M., Pirozzoli, S., Orlandi, P.: The effect of large-scale turbulent structures on particle dispersion in wall-bounded flows. Int. J. Multiphase Flow **51**, 55–64 (2013)
5. Boersma, B.J., Nieuwstadt, F.T.M.: Large-eddy simulation of turbulent flow in a curved pipe. J. Fluid Eng. **118**, 248 (1996)
6. Eaton, J., Fessler, J.: Preferential concentration of particles by turbulence. Int. J. Multiphase Flow **20**, 169–209 (1994)
7. Fischer, P.F., Lottes, J.W., Kerkemeier, S.G.: `nek5000` Web page. http://nek5000.mcs.anl.gov (2008)
8. Gerashchenko, S., Sharp, N., Neuscamman, S., Warhaft, Z.: Lagrangian measurements of inertial particle accelerations in a turbulent boundary layer. J. Fluid Mech. **617**, 255–281 (2008)
9. Huang, X., Durbin, P.: Particulate dispersion in a turbulent serpentine channel. Flow Turb. Combust. **85**(3–4), 333–344 (2010)
10. Huang, X., Durbin, P.: Particulate mixing in a turbulent serpentine duct. Phys. Fluids **24** (2012)
11. Hüttl, T.J., Friedrich, R.: Influence of curvature and torsion on turbulent flow in helically coiled pipes. Int. J. Heat Fluid Flow **21**(3), 345–353 (2000)
12. Hüttl, T.J., Friedrich, R.: Direct numerical simulation of turbulent flows in curved and helically coiled pipes. Comput. Fluids **30**(5), 591–605 (2001)
13. Lavezzo, V., Soldati, A., Gerashchenko, S., Warhaft, Z., Collins, L.: On the role of gravity and shear on inertial particle accelerations in near-wall turbulence. J. Fluid Mech. **658**, 229–246 (2010)

14. Marchioli, C., Giusti, A., Salvetti, M.V., Soldati, A.: Direct numerical simulation of particle wall transfer and deposition in upward turbulent pipe flow. Int. J. Multiphase Flow **29**(6), 1017–1038 (2003)
15. Noorani, A.: Lagrangian particles in turbulence and complex geometries. Tech. rep., KTH, Mechanics. Licenciate Thesis (2014)
16. Noorani, A., El Khoury, G.K., Schlatter, P.: Evolution of turbulence characteristics from straight to curved pipes. Int. J. Heat Fluid Flow **41**, 16–26 (2013)
17. Noorani, A., Sardina, G., Brandt, L., Schlatter, P.: Particle transport in turbulent curved pipe flows. arXiv preprint arXiv:1501.1162513 (2015)
18. Olivieri, S., Picano, F., Sardina, G., Iudicone, D., Brandt, L.: The effect of the Basset history force on particle clustering in homogeneous and isotropic turbulence. Phys. Fluids **26**(041), 704 (2014)
19. Picciotto, M., Marchioli, C., Soldati, A.: Characterization of near-wall accumulation regions for inertial particles in turbulent boundary layers. Phys. Fluids **17**(098), 101 (2005)
20. Portela, L., Cota, P., Oliemans, R.: Numerical study of the near-wall behaviour of particles in turbulent pipe flows. Powder Tech. **125**(2), 149–157 (2002)
21. Reeks, M.W.: The transport of discrete particles in inhomogeneous turbulence. J. Aerosol Sci. **14**(6), 729–739 (1983)
22. Sardina, G., Schlatter, P., Brandt, L., Picano, F., Casciola, C.M.: Wall accumulation and spatial localization in particle-laden wall flows. J. Fluid Mech. **699**, 50–78 (2012)
23. Sardina, G., Schlatter, P., Picano, F., Casciola, C.M., Brandt, L., Henningson, D.S.: Self-similar transport of inertial particles in a turbulent boundary layer. J. Fluid Mech. **706**, 584–596 (2012)
24. Schiller, L., Naumann, A.: Über die grundlegenden Berechnungen bei der Schwerkraftaufbereitung. Ver. Deut. Ing. **77**, 318–320 (1933)
25. Toschi, F., Bodenschatz, E.: Lagrangian properties of particles in turbulence. Annu. Rev. Fluid Mech. **41**, 375–404 (2009)
26. Vashisth, S., Kumar, V., Nigam, K.: A review on the potential applications of curved geometries in process industry. Ind. Eng. Chem. Res. **47**(10), 3291–3337 (2008)
27. Vinkovic, I., Aguirre, C., Ayrault, M., Simoëns, S.: Large-eddy simulation of the dispersion of solid particles in a turbulent boundary layer. Bound.-Layer Meteorol. **121**(2), 283–311 (2006)
28. Wu, Z., Young, J.B.: The deposition of small particles from a turbulent air flow in a curved duct. Int. J. Multiphase Flow **44**, 34–47 (2012)
29. Yeo, K., Kim, B., Lee, C.: On the near-wall characteristics of acceleration in turbulence. J. Fluid Mech. **659**, 405–419 (2010)
30. Young, J., Leeming, A.: A theory of particle deposition in turbulent pipe flow. J. Fluid Mech. **340**(1), 129–159 (1997)
31. Zamansky, R., Vinkovic, I., Gorokhovski, M.: Acceleration statistics of solid particles in turbulent channel flow. Phys. Fluids **23**(11), 113,304 (2011)
32. Zonta, F., Marchioli, C., Soldati, A.: Particle and droplet deposition in turbulent swirled pipe flow. Int. J. Multiphase Flow **56**, 172–183 (2013)